PAPR Reduction of OTSM with Random and Orthogonal SLM Phase Sequences and its Recovery in the Presence of EPA, EVA and ETU Channel Models

Mohammed I. AL-RAYIF

Dept. of Applied of Electrical Engineering, College of Applied Engineering, King Saud University, Almuzahmia Branch, P.O. Box 800, 11421 Riyadh City, Saudi Arabia

malrayif@ksu.edu.sa

Submitted August 10, 2024 / Accepted October 31, 2024 / Online first November 12, 2024

Abstract. *To overcome the high peak-to-average-power ratio (PAPR) in orthogonal time sequency multiplexing (OTSM), this document proposes orthogonal and random selective mapping phase vectors (OSLM and RSLM) after some modifications to be applicable with OTSM constructions at both transmitter and receiver. Consequently, the PAPR (without explicit side information) of the original phase vectors is reduced and restored in the presence of a nonlinear power amplifier, and three different multipath fading channel models: Extended pedestrian A (EPA), Extended vehicular A (EVA) and Extended typical urban (ETU), with different user speed, namely* 150 *and* 500 *km/h. Also, complementary cumulative distribution function (CCDF) PAPR comparisons are provided based on the Walsh Hadamard transform (WHT) matrix $\boldsymbol{W}_N$ and the inverse symplectic fast Fourier transform (ISFFT) matrix $\boldsymbol{F}_N$. Furthermore, three detectors are modified and implemented in this work, namely single tap MMSE (ST-MMSE), Gauss-Seidel iterative matched filter (MFGS) and linear MMSE (LMMSE). As a result, this proposal shows reliable performance in terms of PAPR reduction, bit error rate (BER) and side information error rate (SIER) of the OTSM system at a fraction of extension values ($f = 0.09$ and $C = 1.15$) while maintaining power efficiency.*

Keywords

PAPR, SLM, OTFS, OTSM, LMMSE, single-tap MMSE, Gauss-Seidel iterative matched filter

1. Introduction

Orthogonal time sequency multiplexing (OTSM) modulation is a two-dimensional (2D) modulation scheme in which information symbols are multiplexed in a delay-sequence domain, where the sequency is defined as the number of zero crossing per unit time interval. In other words, OTSM is a combination of sequency multiplexing and time division multiplexing [1–3]. OTSM performs similar to more advanced modulation schemes in the literature such as orthogonal time frequency space modulation (OTFS), while OTSM outperforms the latter in terms of complexity due to the use of WHT, instead of Fourier transform (ISFFT) [2–6], while maintaining the BER performance identical to that of OTFS. Therefore, the OTSM was considered as the starting point for this work. However, as with any multicarrier system, OTSM suffers from the high peak-to-average power ratio (PAPR). The high PAPR results in signal distortion when passing through the nonlinear high power amplifier (HPA) where the peak that is above the saturation point of HPA will be clipped. This phenomenon will introduce out-of-band radiation and in-band distortion, which, in turn, reduces the system's overall performance [7]. Hence, several solutions have been presented in the literature to overcome this problem, although they are still limited compared to those presented for OFDM PAPR reduction. Below, we present an introduction to the most recent and most efficient studies in the literature ,which are mainly related to the high PAPR processing of OTSM/OTFS.

In [8], the authors analyzed the PAPR of OTFS waveform. They consider modulation symbols on an $N \times M$ delay-Doppler grid, where N is the number of Doppler bins and M is the number of delay bins. In their view, the upper limit of the PAPR of an OTFS signal is limited by the maximum PAPR that grows linearly with N (and not with M, the number of subcarriers). Despite this analysis, however, the CCDF-PAPR is usually accounted at the end of the ISSFT multicarrier process with a one-dimensional OTFS frame ($MN \times 1$). Therefore, M will affect, even slightly, the PAPR performance, especially when using the embedded pilot delay-time channel estimation [4]. Furthermore, a new sequence indexing method referred to as pairwise sequence index modulation (PSeIM) was introduced in [9] to address SeIM issues for robustness and energy efficiency in SeIM-based communication systems. In PSeIM, errors are prevented without having to apply on-off keying (OOK)

DOI: 10.13164/re.2024.0744

thresholding, by encoding information across pairs of sequences. Based on their proposal, the PSeIM-OTSM outperforms OTSM in terms of BER, energy efficiency, and PAPR with a lower implementation complexity. However, since they introduce $M \times N/2$ inactivated sequence bins of the OTSM matrix, it means that non-data has been allocated in this part of the matrix, so the PAPR will be reduced to 50%. In other words, the PAPR reduction obtained in their proposal is equivalent, in some way, to reducing the size of OTSM matrix by half. For high values of N ($N > 4$), a conventional μ-law companding technique is presented in [10]. They demonstrated a gain of OTFS-PAPR reduction up to 2.5 dB over the original OTFS signal with slight degradation in bit error rate (BER) performance. Also, an analysis of PAPR reduction techniques has been provided in [11] for adapted tone reservation (TR) in OTSM system performance. In [12], the PAPR is analyzed and minimized using the superimposed pilot scheme compared to conventional zero padded (ZP) pilot scheme. Additionally, a discrete cosine transform (DCT)-based OTFS is presented in [13]. This scheme shows about 20% PAPR reduction (in the upper limit of the PAPR for conventional OTFS) and less complexity without compromising bit error rate (BER) performance. DCT-OTFS also shows an approximate 0.5 dB reduction in the CCDF-PAPR compared to conventional OTSM. In [14], a nonlinear corrective active constellation expansion (NC-ACE) method in OTFS waveform is proposed. Due to the nonlinear compression characteristics, an accurate control of PAPR and BER performance is reached. The peak windowing technique is used in [15] to reduce the OTFS-PAPR for high-speed railways in order to achieve reliable communication in IoT for railways (IoT-R). Furthermore, a PAPR reduction method is studied in the pilot-embedded OTFS modulation by [16], where the interference between data and pilot symbols is avoided by using guard symbols with zero padding. This method provided efficient PAPR reduction, although its BER shows a short deviation from the original OTFS-BER performance. Based on precoded methods, [17] and [18] show that using the precoder in OTFS leads to a significant PAPR reduction, while introducing an increasing in errors at some conditions. In addition to that, two alternative channel estimation scenarios are proposed in [19] for static multipath channels based on a low PAPR preamble, which is defined in the delay-Doppler domain. Despite it illustrates a remarkable increase in the PAPR when increasing the header value x_p, they reported that their proposal increases the robustness of the OTFS system to nonlinearity and allows a higher power efficiency. In terms of distortion-free techniques, used to minimize PAPR, selective mapping (SLM) and partial transmission sequencing (PTS) are the most common, where the original phases are rotated into selected new phases and then only the modified data frame that offers the minimum PAPR is selected. The latter approach, PTS, is suggested by [7]. The authors introduce PTS based on the center phase sequence matrix (CPSM) to reduce the rate of PAPR. It showed a significant reduction in the PAPR while maintaining the BER and PSD performance, although no information was provided about the assumed power amplifier (if applicable), channel and the recovery design to obtain the original phases. Moreover, a normalized SLM grouping (NSLM) is proposed in [20] to reduce the system OTFS-PAPR. μ-NSLM is proposed by combining the NSLM with the μ-LAW companding algorithm, which further reduces the PAPR of the system. However, it does not provide any discussion about the BER performance. In [21], the PAPR performance in OTFS modulation is analyzed using classical SLM, without any discussions about the system's BER performance. Finally, [22] introduces a metric-based symbol predistortion algorithm, to reduce the PAPR in OTFS modulation. This algorithm is constrained by error vector magnitude (EVM) limits. However, this scheme induces distortion of OTFS frames, which leads to an increase in the bit error rate of the system.

In this proposal, the distortionless SLM approach is presented in two approaches (the orthogonal-SLM (OSLM) [23] and the random-SLM (RSLM) [24]) with appropriate modifications to be applicable with OTSM modulation, to reduce its PAPR. These approaches are implemented in the presence of different models of multipath fading channel, that are extended pedestrian A (EPA), extended vehicular A (EVA) and extended typical urban (ETU). Besides that, three different detectors are applied, namely single tap minimum mean squared error (ST-MMSE) [25], Gauss-Seidel iterative matched filter (MFGS) [2, 3, 26] and Linear MMSE (LMMSE) [4]. Therefore, the main objective of this study is to reduce the PAPR of OTSM modulation while maintaining BER performance. Because OSLM and RSLM are based on the principle of rotating original phases to other specific phases, a reliable recovery process, at each detector, has been appropriately designed to be able to convert the received data back to its original phase. This can be considered as another goal of this proposal. The main concept of this proposal is to generate U-phase vectors (either orthogonally or randomly) to obtain U-copies of the OTSM frame. Hence, the frame of the OTSM version with the lowest PAPR is considered to transmit and pass through the nonlinear power amplifier (NLPA) (the solid-state power amplifier (SSPA) [27] model is applied in this proposal). At the receiver, the transmitted phase vector is recognized at each detector by the proposed recovery process, and proceeding in data estimation. This recovery process is implemented by introducing a specific metric that has been adapted from [23]. The contributions of this work are listed as follows:

- OTSM system of [2], [3] has been modified to be able to work with the proposed PAPR reduction schemes at both the transmitter and the receiver. In terms of the proposed PAPR reduction techniques, the OSLM and RSLM have been modified to shift the original data in both phase and magnitude, where the latter is being partially shifted. Additionally, the transmitted OSLM/RSLM phase vector $\mathbf{P}_{\mathrm{v}}$ is recovered at the receiver side by modifying the OTSM detectors with a certain numerical counter Γ. This has been implemented with three detectors and all show excellent results.

- The SSPA is implemented as a nonlinear power amplifier and affects the system performance, which is ignored in most of the methods available in the literature.
- The power efficiency of the proposed OSLM and RSLM is analyzed, and the best adjustment values for the extension factors (C and f) are determined based on the desired power efficiency.
- Three models of multipath fading channel (EPA, EVA and ETU), with different user's velocity, are considered, and an acceptable system performance is obtained.
- As a result, this proposal provides a reliable comparison in terms of CCDF-PAPR, BER and SIER performances at different circumstances of input factors such as, for example, $M \times N$ size, size of M-QAM, SSPA input-back-off (IBO), U phase vectors, values of extended factors C and f, speed of user (km/h) and EPA, EVA and ETU channel models,etc.

The rest of the paper is organized as follows. In Sec. 2, we present the OTSM system model in the presence of the proposed PAPR reduction schemes followed by the simulation results and discussions in Sec. 3. Finally, we end this study with the conclusion.

2. System Model

Figure 1 and Figure 4 show the block diagram of OTSM modulation and demodulation, respectively, with the proposed PAPR reduction architecture. At the OTSM transmitter, the information symbols (e.g., QAM/PSK symbols) are processed in two-dimensional delay-sequency (DS) matrix and are modified to a new phase via the generated selective mapping (SLM) matrix then mapped to the delay-time (DT) plane through the 2D Walsh Hadamard transform matrix WHT (which is also equivalent to ISFFT proposed in [4]). The obtained 2D DT signal is then transferred to the time-domain samples $\mathbf{S}$ by column-wise vectorizing and the cyclic prefix (CP) is added. Next it is passed through the counting PAPR ratio processor and, hence, the modified $\mathbf{s}$ vector which introduces the lowest PAPR is considered for transmission into the physical channel after passing through the NLPA (SSPA). Moreover, at the receiver side, the three detectors ST-MMSE, LMMSE and IMFGS are developed with the recovery process to identify the desired phase vector, then proceeding to estimate the transmitted data symbols (QAM).

Accordingly, from [2–4], consider $\mathbf{s}, \mathbf{r} \in \mathbb{C}^{MN\times 1}$ be the transmitted and received information symbols. The total frame duration and bandwidth of the transmitted OTSM signal frame are $T_\mathrm{f} = NT$ and $B = M\Delta f$, respectively, where $\Delta f = 1/T$, i.e., the signal is critically sampled for any pulse shaping waveform, and N is chosen to be a power of 2. In the following subsections, models of transceiver, channel and input-output relation are proposed with the proposed PAPR minimization (SLM) technique based on the recently mentioned proposals.

2.1 OTSM Transmitter

Figure 1 shows the proposed OTSM transmitter operation. The information symbols $\mathbf{X} = \left[\mathbf{X}_0^\mathrm{T}, \ldots, \mathbf{X}_{M-1}^\mathrm{T}\right]^\mathrm{T}$ are split into vectors $\mathbf{X}_m \in \mathbb{C}^{N\times 1}$, $m = 0, \ldots, M-1$. The symbol vectors are modified by a generated phase vector $\mathbf{P}_u = \left[p_{u,0}, \ldots, p_{u,N-1}\right]$, where $p_u \in \mathrm{e}^{\mathrm{j}\pi r}$ and $u = 0, 1, \ldots, U-1$ where r is any integer value. These phase vectors $[\mathbf{P}_0, \ldots, \mathbf{P}_u, \ldots, \mathbf{P}_{U-1}]$ are generated either randomly (RSLM) (by applying r randomly) or orthogonally (OSLM) (by applying the Walsh Hadamard matrix $[N \times N]$) and select any U vectors/rows where the first row is excluded (as will be demonstrated in Sec. 2.1.1 and Sec. 2.1.2 to produce the modified symbol vectors $\mathbf{X}_{u,m}$. The symbol vectors are arranged into a matrix $\mathbf{X}_u \in \mathbb{C}^{M\times N}$ by placing each symbol vector $\mathbf{X}_{u,m}$ in the m-th row. The column and row indices represent the delay and sequency indices, respectively, of the delay-sequency grid.

$$\mathbf{X}_u = \left[\mathbf{X}_{u,0}, \mathbf{X}_{u,1}, \ldots, \mathbf{X}_{u,M-1}\right]^\mathrm{T}. \tag{1}$$

A N-point Walsh-Hadamard transform matrix (WHT) $\mathbf{W}_N$ is applied on each of these symbol vectors to transform it to the delay-time domain,

$$\mathbf{x}_u = \mathbf{X}_u \cdot \mathbf{W}_N = \left[\mathbf{x}_{u,0}, \mathbf{x}_{u,1}, \ldots, \mathbf{x}_{u,M-1}\right]^\mathrm{T}. \tag{2}$$

The matrix $\mathbf{x}_u$ is column-wise vectorized to obtain the time-domain samples $\mathbf{S}_u \in \mathbb{C}^{MN\times 1}$ to formulate it as in [2]

$$\mathbf{S}_u = \mathrm{vec}\left(\mathbf{x}_u\right). \tag{3}$$

The time-domain sample is next passed through the counter of lowest PAPR for all U trials to consider the corresponding time-domain sample $\mathbf{s}_u$ for transmission. After adding cyclic prefix (CP) (with the length equal to or greater than the maximum discrete delay spread index l_max of the channel), the sample is passed through the nonlinear power amplifier. The SSPA (Rapp Model) [27] is assumed in this proposal. Lastly, the pulse shaping and digital-to-analog conversion is applied to transmit the sample into the wireless channel as $s_u(t)$. The following subsections present a description and analysis of the PAPR reductions methodologies, design of SSPA, OSLM and RSLM constructions and zero padding principle.

2.1.1 PAPR Reduction and NLPA

Consider a single modified time-domain samples vector $\mathbf{S}_u$, $u = 0, 1, \ldots, U-1$, where U is the maximum number of generated phase vectors, and $\mathbf{P}_u = \left[p_{u,0}, p_{u,1}, \ldots, p_{u,N-1}\right]$ with $p_{u,n}$ is a generated phase element which is either $+1$ or -1. After generating the (DS) matrix, for each mth row, each element $p_{u,n}$ is multiplied by the corresponding complex symbol $X_{m,n}$. Subsequently, all processes are applied as mentioned above until we reach the time-domain samples

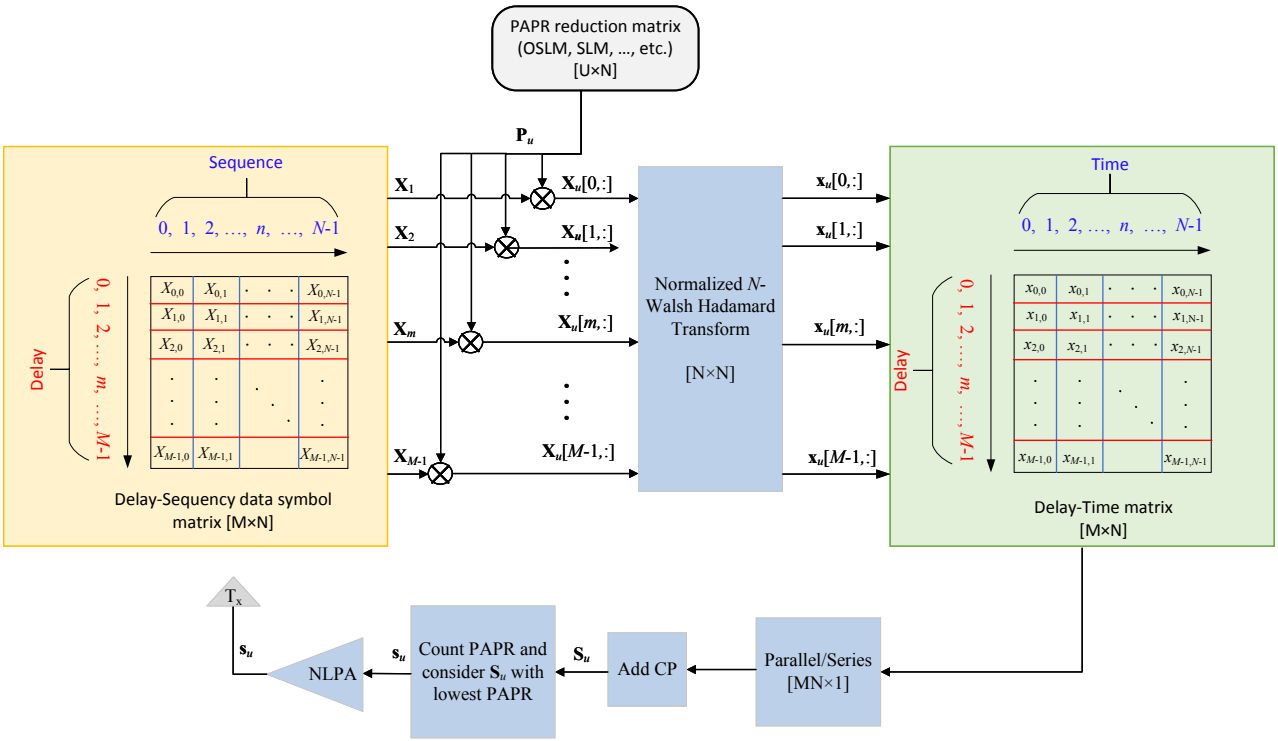

Fig. 1. The block diagram of the proposed OTSM transmitter.

vector $\mathbf{S}_u \in \mathbb{C}^{MN\times 1}$, where its PAPR is calculated as follows

$$\text{PAPR}_u = \frac{\max\limits_n \left\{|S_u(n)|^2\right\}}{\text{E}\left\{|S_u(n)|^2\right\}} \tag{4}$$

where $\text{E}\{\cdot\}$ is the expectation operation, i.e. the average power of $\mathbf{S}_u$ in (4). This process is applied to all candidate phase vectors U to introduce different PAPR values. The $\mathbf{S}_u$ vector with the lowest PAPR ratio $\mathbf{s}_u$ is forwarded to the following processes, then transmitted over the physical channel. It is worth mentioning that the PAPR ratio is affected proportionally by the dimensions of N and M, as is analyzed in [8] though they approved that the PAPR grows linearly with M, contrary to what they observed in their results where the dimension N made sense, even though a fraction. The theoretical CCDF (with rectangular pulse) of the PAPR of OTSM is then expressed as [8]

$$P(\text{PAPR} > \gamma_0) = 1 - (1 - \text{e}^{-\gamma_0})^{MN} \tag{5}$$

where $P(\text{PAPR} > \gamma_0)$ is the probability that the PAPR exceeds a given threshold γ_0. Hence, for U trials, the CCDF-PAPR is given by

$$\begin{aligned} P(\text{PAPR} > \gamma_0) &= \prod_{u=0}^{U-1} \left(1 - (1 - \text{e}^{-\gamma_0})^{MN}\right) \\ &= \left(1 - (1 - \text{e}^{-\gamma_0})^{MN}\right)^U. \end{aligned} \tag{6}$$

Further, a CP (of length $\geq l_{\max}$) is added to the time-domain signal $\mathbf{S}_u$ (containing the pilot sample, if applicable), to assist in the channel estimation process. The CP is added to the start of the frame by copying the last ($\mathbf{x} \in \mathbb{C}^{M\times 1}$) samples of the time-domain frame. This CP is removed, at the receiver front-end, from the received signal $\mathbf{r}$. Lastly, the frame $\mathbf{s}_u$ is passed through the NLPA, specifically the SSPA with the following related nonlinear transformation [27], [28]

$$\mathcal{A}\left[|\mathbf{s}_u|\right] = \frac{K_1|\mathbf{s}_u|}{\left[1 + \left(\frac{K_1|\mathbf{s}_u|}{A_\text{o}}\right)^{2\rho}\right]^{\frac{1}{2\rho}}}, \quad \Phi\left[|\mathbf{s}_u|\right] = \alpha_\varphi \left(\frac{K_1|\mathbf{s}_u|}{A_\text{o}}\right)^4 \tag{7}$$

where $A_\text{o} = \sqrt{\text{IBO} \cdot \text{E}\{\mathbf{s}_u\}}$ is the saturating amplitude at a specific *input-back-off* (IBO), K_1 is the small signal gain (and is ignored in this study), ρ is a parameter which controls the smoothness of the transition from the linear region to the saturation region (which is set to 3 in this study), and α_φ is usually set to zero, which means that SSPA does not add any phase distortion. The output time-domain frame of the SSPA is denoted by $\mathbf{s}_u$ and is then transmitted.

2.1.2 Construction of Orthogonal-SLM and Random-SLM

In Orthogonal-SLM (OSLM), the generated phase vectors are mutually orthogonal, while in Random-SLM (RSLM) they are not. For OSLM, the 2D Walsh-Hadamard matrix (WHM) $[N \times N]$ is generated, then only U rows are selected from the matrix as the candidate phase vectors $\mathbf{P}_u = [1 \times N]^\text{T}$, where $u \in [2, \ldots, N-1]$, i.e. the first row of WHM is excluded because the phase sequence in this row introduces non modification phases. Hence, we will have

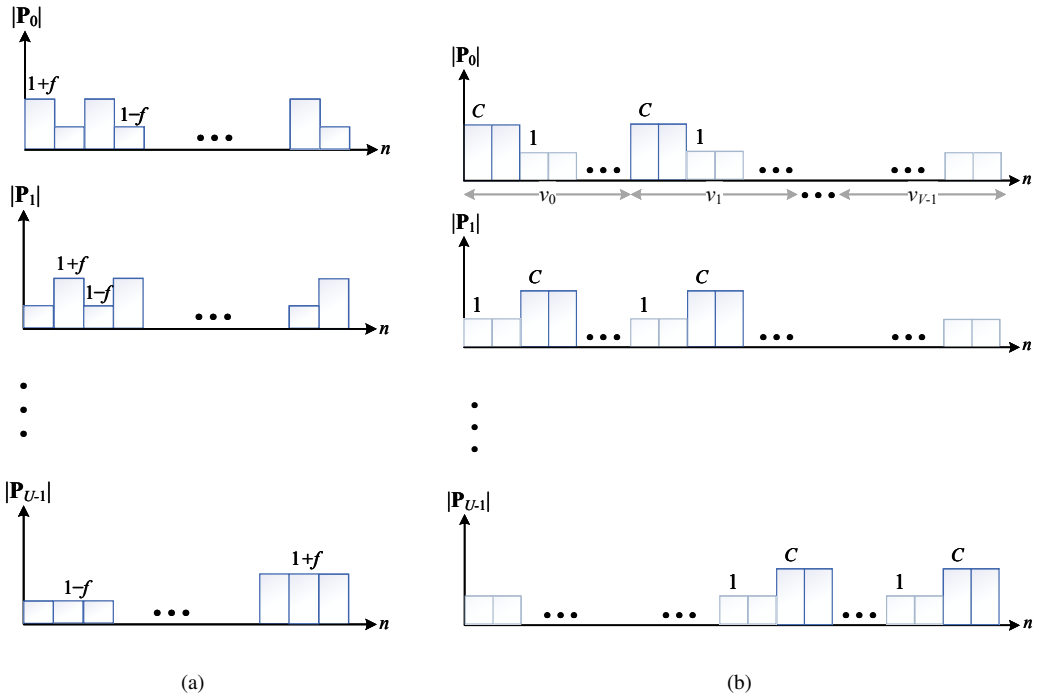

(a) (b)

Fig. 2. The constructions of (a) OSLM and (b) NSLM phase vectors.

$\mathbf{P} = \left[\mathbf{P}_0^{\mathrm{T}}, \ldots, \mathbf{P}_{U-1}^{\mathrm{T}}\right]^{\mathrm{T}}$ and $\mathbf{P}_u = \left[p_{u,0}, p_{u,1}, \ldots, p_{u,N-1}\right]$ for $p_{u,n} \in [-1, +1]$. On the other side, the RSLM vectors are generated randomly with the same dimension $[U \times N]$ as the overall selected orthogonal vectors. To identify the phase vector $\mathbf{P}_{\mathrm{v}}$ which is combined with the transmission data at the lowest PAPR, such that the received information can be recovered to the original phases, we introduce an extension factor $0 < f < 0.5$ in OSLM vectors, to extend/shrink a specific element $p_{u,n}$, and $1 < C < 1.5$ in RSLM vectors, to extend the element $p_{u,n}$, as follows

- For OSLM: The principle of [23] is considered with the modification expressed in (8)

$$\mathbf{P}_u + f = \left[p_{u,0}, p_{u,1}, \ldots, p_{u,N-1}\right] + f. \tag{8}$$

  Consequentially, from (8), each obtained phase element with +1 is increased fractionally while decreased at each −1 element, where the maximum deviation between $+1+f$ and $-1+f$ is equivalent to $2f \ll 1$ (see Fig. 2(a)). This design plays two important roles: Firstly, changing the phases of a specific complex symbol when multiplying by the corresponding negative element $-1 + f$. Secondly, changing the magnitude of the corresponding symbol. So, it helps to identify the desired phase vector $\mathbf{P}_{\mathrm{v}}$ based on the modified values, which were orthogonally distributed, as will be demonstrated later.

- For RSLM: The principle of the RSLM construction is adapted from [24]. Each generated RSLM vector is divided into V subvectors and inside each subvector, α elements are extended to $1 \leq |C| \leq 1.5$. In this scenario, the extension factor can be implemented at either +1 or −1 elements, however these extended elements are orthogonally distributed with respect to the extended elements in other candidate vectors (see Fig. 2(b)).

It is important to discuss the effect of these extension factors on the transmitted power. To simplify, suppose a single sequency row $\mathbf{X}_u[m]$, hence, by subtracting the non-extended frame from the corresponding extended one, the extended power E_i can be determined. As a result, for RSLM frame, $E_{i,\mathrm{RSLM}}$ can be formulated as

$$\begin{aligned} E_{i,\mathrm{RSLM}} &= |\mathbf{X}_u[m]|^2 - |\mathbf{X}[m]|^2 \\ &= \left[\left(\alpha V C^2 E_{\mathrm{s}}\right) + \left(\left(\frac{N}{V} - \alpha\right) V E_{\mathrm{s}}\right)\right] - N E_{\mathrm{s}} \\ &= \alpha E_{\mathrm{s}} V \left(C^2 - 1\right) \end{aligned} \tag{9}$$

where E_{s} is the symbol energy and α is referred to the number of extended elements per subvector V (for more information, see [24]). On the other hand, for the OSLM, the power per sequency frame increases at $1 + f$ (i.e. > 1) while decreases at $-1 + f$ (i.e. < 1), taking into consideration that, due to orthogonality distribution of WH matrix, the number of elements with additional power is equal to that with reducing power, and each is equivalent to $N/2$. Therefore, the obtained power by OSLM frame $E_{i,\mathrm{OSLM}}$ can be determined as

$$\begin{aligned} E_{i,\mathrm{OSLM}} &= |\mathbf{X}_u[m]|^2 - |\mathbf{X}[m]|^2 \\ &= \left[\left(\frac{N}{2} E_{\mathrm{s}} (1+f)^2\right) + \left(\frac{N}{2} E_{\mathrm{s}} (-1+f)^2\right)\right] - N E_{\mathrm{s}} \\ &= N E_{\mathrm{s}} f^2. \end{aligned} \tag{10}$$

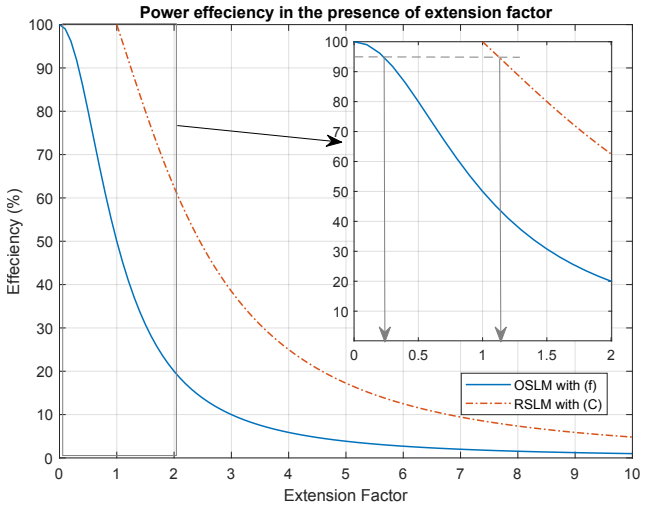

Fig. 3. Power efficiency versus extension factor (f and C) at $E_s = 1$.

Finally, the efficiency power (per m sequency frame) in attendance of extension factors f for OSLM and C for RSLM, is expressed, respectively, as

$$\eta_{\text{OSLM}}\% = \frac{P_{\text{org}}}{P_{\text{OSLM}}} = \frac{NE_s}{NE_s\left(1+f^2\right)} = \frac{1}{\left(1+f^2\right)}, \tag{11}$$

$$\eta_{\text{RSLM}}\% = \frac{P_{\text{org}}}{P_{\text{NSLM}}} = \frac{NE_s}{NE_s + \alpha E_s V\left(C^2-1\right)} \tag{12}$$

where P_{org} is referred to the original power (i.e., without any additional power). Hence, at $f = 0$ in (11) and $C = 1$ in (12) the resultant efficiency power will be 100%. For instance, at $f = 0.22$ and $C = 1.3$ (consider $N = 10$, $E_s = 1$ $V = N/5 = 2$ and $\alpha = 2$), hence $\eta_{\text{OSLM}} = 95.4\%$ and $\eta_{\text{RSLM}} = 78.37$. It indicates that the OSLM technique is more efficient than RSLM. Figure 3 shows the characteristic of power efficiency versus extension factors, that are f for OSLM and C for RSLM, supposing $E_s = 1$. From the figure, it can be observed that the efficiency decays dramatically when extension factor increases. Hence, to achieve at least ($\approx 95\%$) of power efficiency, f must be adjusted at about 0.225 while C at 1.15 approximately, under the assumption that $E_s = 1$.

Notice that the 100% efficiency is the best case, so we need to be close as much as possible to this percentage. So, from Fig. 3, we considered the values of extension factors for which the power efficiency is not less than 95% (i.e. $f = 0.09$ and $C = 2f$). Consequentially, the transmitted power will contain the original power besides the extended power (E_i), with a very small modification, which was produced by the extension factors, hence the SNR will be considered mostly unchanged.

2.1.3 Zero Padding (ZP) and Pilot Samples Insertion

Based on the proposal of [2], [3], the last $2l_{\max}+1$ rows of $\mathbf{X} \in \mathbb{C}^{M\times 1}$ are set to zero to enable insertion of pilot and guard samples, where $l_{\max}$ indicates the maximum delay spread of the channel. Zero samples act as interleaved zero padding (ZP) between the time domain blocks. These ZPs prevent interference between blocks and interference between data and pilots, so process of detection and channel estimation become easier. Moreover, the process of adding CP to the time domain signal helps in the channel estimation process. However, in this study, the ZP technique is implemented excluding insertion of pilots because the channel is supposed to be known perfectly at the receiver, given that channel estimation is out of the spotlight of this study's subject. Due to channel delay spread, samples leak from block $(n-1)$ to block n, which is introduced as inter-block-interference. This interference can be overcome by assuming $\mathbf{0}_N$ empty symbol vectors along the last rows $l_{\max}$ of $\mathbf{X}$ (i.e., ZP is applied along the delay dimension of the OTSM matrix). Hence, as proposed in [2], [3], we can set

$$\mathbf{X}_m[n] = \mathbf{x}_m[n] = \mathbf{0}, \quad \text{if } m \geq M - l_{\max}. \tag{13}$$

2.2 Discrete Time Baseband Channel Model and Input-Output Relation

This section is presented, without any modification, as that in [2], [3], where the channel is considered, in this work, to be known perfectly to the receiver. At the end-side of the transmitter, the time-domain signal $\mathbf{s}_u$ is split into N time-domain blocks as $\mathbf{s}_u = \left[\mathbf{s}_{u,0}^{\text{T}}, \ldots, \mathbf{s}_{u,N-1}^{\text{T}}\right]^{\text{T}}$. Whereas the relationship between the M samples of the time-domain blocks $\mathbf{s}_{u,n}$ and the delay-time symbol vectors $\mathbf{x}_{u,m}$ is equivalent, and can be expressed as

$$\mathbf{s}_{u,n}[m] = \mathbf{x}_{u,m}[n]. \tag{14}$$

As is known, the discrete baseband channel array $\mathbf{G} \in \mathbb{C}^{NM\times NM}$, in delay time, destroys the transmitted signal $\mathbf{s}_u$, so that the received time domain signal $\mathbf{r} = \mathbf{G}\cdot\mathbf{s}$ is obtained. At the receiver station, by splitting the received signal $r(t)$ at $t = q/M\Delta f$, where $0 \leq q \leq NM-1$, the discrete time model is achieved. Now, suppose the set of discrete delay taps $\mathcal{L} = [0, \ldots, l_{\max}]$, which represents the delay shifts at integer multiples of the sampling period $1/M\Delta f$. Also, given that the discrete channel $g^{\text{s}}[l,q] = g(\tau,t)$ at $\tau = l/M\Delta f$ and $t = q/M\Delta f$, where g_i, τ_i and v_i are the complex path gain, the delay-shift and the Doppler-shift, respectively, associated with the i-th path (with P is the maximum number of channel paths). By applying the sampling theorem to the delay-time channel $g(\tau,t) = \sum_{i=1}^{P} g_i e^{\text{j}2\pi v_i(t-\tau_i)}$, hence, at discrete delay taps $l \in \mathcal{L}$, the discrete baseband delay-time channel can be formulated as

$$g^{\text{s}}[l,q] = \sum_{i=1}^{P} g_i \mathcal{Z}^{\mathcal{K}_i(q-l)}\delta[l-L_i] \tag{15}$$

where $\mathcal{Z} = e^{\text{j}2\pi/NM}$, $\mathcal{K}_i$ and L_i are the normalized delay shift and Doppler shift, respectively, associated with the i-th path, such that $\tau_i = L_i/M\Delta f$ and $v_i = \mathcal{K}_i/NT$. Considering that, in common practice, the fractional path delays L is rounded to the nearest integer multiple of the sampling interval $1/M\Delta f$, i.e., $L_i \in \mathbb{Z}$. Furthermore, when sampling the

transmitted and received time-domain signals at $t = q/M\Delta f$, the received discrete time-domain input-output relation can be expressed as

$$\mathbf{r}[q] = r\left(\frac{q}{M\Delta f}\right) = \sum_{l\in\mathcal{L}} g^{\mathrm{s}}[l,q]\,\mathbf{s}_u[q-l] + \mathbf{W}[q] \quad (16)$$

where $\mathbf{s}_u[q] = s_u[q/M\Delta f]$ and $\mathbf{W}[q]$ is the additive white Gaussian noise (AWGN) with variance σ_{w}^2. The input-output relation $\mathbf{r}_n[m]$ will introduce an inter-block-interference after splitting the discrete time index $q = 0, 1, \ldots, MN-1$, in terms of the delay and sequency frame indices as $q = m+nM$, where the $m = 0, 1, \ldots, M-1$ and $n = 0, 1, \ldots, N-1$. By ignoring the AWGN noise, this input-output relation can be formulated as

$$\mathbf{r}_n[m] = \sum_{l,l\le m} g^{\mathrm{s}}[l, m+nM]\,\mathbf{s}_{u,n}[m-l] + \underbrace{\sum_{l,l>m} g^{\mathrm{s}}[l, m+nM]\,\mathbf{s}_{u,n-1}[[m-l]_M]}_{\text{inter-block-interference}}. \quad (17)$$

This interference can be removed by using ZP and setting $\mathbf{s}_{u,n}[m] = 0$ for all n when $m \ge m - l_{\max}$, so that the second term in (17) disappears.

2.3 Detection Process and OSLM/NSLM Phase Vector Recovery

After CP removal, from [2], [3], the time-domain vector $\mathbf{r} \in \mathbb{C}^{NM\times 1}$ is obtained, where the interference between time domain blocks is canceled, thanks to ZP process. This enables the time-domain input-output relation in (3) to be partitioned into $\mathrm{vec}_{M,N}^{-1}(\mathbf{r})$ matrices and treated independently (as illustrated in Fig. 4) as follows

$$\mathbf{r}_n = \mathbf{G}_n \cdot \mathbf{s}_{u,n} + \mathbf{W}_n, \quad n = 0, 1, \ldots, N-1 \quad (18)$$

where $\mathbf{s}_u = \left[\mathbf{s}_{u,0}^{\mathrm{T}}, \ldots, \mathbf{s}_{u,N-1}^{\mathrm{T}}\right]^{\mathrm{T}}$, and $\mathbf{r} = \left[\mathbf{r}_0^{\mathrm{T}}, \ldots, \mathbf{r}_{N-1}^{\mathrm{T}}\right]^{\mathrm{T}}$ and $\mathbf{G}_n$ referred to the channel at the n-th time-domain block. Although the time-domain channel matrix is no more circulant due to the time-varying channel, however, since the duration of each time-domain block is small compared to the whole frame, the channel can be assumed to be time-invariant in each block but varying from block to block [3]. The advantage is that, this allows the use of a single-tap-MMSE equalizer for detection in each block followed by the WHT to combine the block estimates. Additionally, by processing the M-point fast Fourier transform (FFT) operation ($\mathbf{F}_M$) on the received blocks (i.e. ISFFT operation), the received time-frequency samples can be acquired as

$$\bar{\mathbf{r}}_n = \mathbf{F}_M \cdot \mathbf{r}_n. \quad (19)$$

Consequently, each n-th block can be equalized in parallel as

$$\bar{\mathbf{s}}_{u,n} = \frac{\bar{\mathbf{h}}_n^*(m)\cdot\bar{\mathbf{r}}_n(m)}{|\bar{\mathbf{h}}_n(m)|^2 + \sigma_{\mathrm{w}}^2} \quad (20)$$

for $m = 0, 1, \ldots, M-1$, $n = 0, 1, \ldots, N-1$ and the AWGN noise variance of σ_{w}^2. Where the frequency domain channel coefficients for each time-domain block are $\bar{\mathbf{h}}_n = \mathrm{diag}\left[\mathbf{F}_M \cdot \mathbf{G}_n \cdot \mathbf{F}_M^{\dagger}\right]$. The information symbol estimates in the delay-sequency domain can then be obtained by the M-point IFFT operation (i.e. SFFT operation) on the time-frequency domain estimates $\bar{\mathbf{s}}_{u,n}$ followed by the N-point WHT as

$$\hat{\mathbf{X}}_u = \mathbf{F}_M^{\dagger} \cdot \bar{\mathbf{s}}_{u,n} \cdot \mathbf{W}_N \quad (21)$$

where $\bar{\mathbf{s}}_{u,n} = \left[\bar{\mathbf{s}}_{u,0}, \bar{\mathbf{s}}_{u,1}, \ldots, \bar{\mathbf{s}}_{u,N-1}\right]$ and $\hat{\mathbf{X}}_u \in \mathbb{C}^{M\times N}$. At this stage, the phase vector recovery process is applied to detect the desired phase vector $\mathbf{P}_{\mathrm{v}}$ from the matrix of phase vectors OSLM or RSLM. As a contribution of this study, the operation of [23] has been modified, to identify the vector $\mathbf{P}_{\mathrm{v}}$, as

$$\Gamma = \max_u \sum_{m\in M} \left[|\hat{\mathbf{X}}_u(m)| \cdot |\mathbf{P}_u|^{\mathrm{T}}\right] \quad (22)$$

where $\hat{\mathbf{X}}_u(m) \in \mathbb{C}^{1\times N}$ for all $0 \le u \le U-1$. Hence, the phase vector $\mathbf{P}_u$ which introduces the maximum argument of Γ is considered as the desired phase vector $\mathbf{P}_{\mathrm{v}}$ (i.e.,$\mathbf{P}_{\mathrm{v}} = \mathbf{P}_u\,(\Gamma)$). This obtained phase vector is used to convert the data sequency $\hat{\mathbf{X}}_u$ to its original phases, after removing effect of extension factors f from $\mathbf{P}_{\mathrm{v}}^{\mathrm{OSLM}}$ and C from $\mathbf{P}_{\mathrm{v}}^{\mathrm{RSLM}}$. In this study, three detectors are implemented, that are MFGS, ST-MMSE and LMMSE. At the output of each detection method, the original data sequency m-th block $\hat{\mathbf{X}}$ is obtained by the element-wise recovery process, in the dimension of n, as

$$\hat{\mathbf{X}} = \frac{\hat{\mathbf{X}}_{u,n}}{\mathbf{P}_{\mathrm{v}}} = \frac{\hat{X}_u(m,n)}{p_{\mathrm{v}}(n)}. \quad (23)$$

Briefly, the output of these detectors can be represented as follows. For the ST-MMSE equalizer, no further operation is required except applying (23) to the output of (21) and removing the ZP frame, then the decision making process takes place to replace each input element with the closest QAM symbol (in terms of Euclidean distance), that is $\mathcal{D}\left(\hat{X}(m,n)\right)$. For the LMMSE block detector, each n-th block (for $0 \le n \le N-1$) is processed such that the estimated data-sequency is expressed as

$$\hat{\mathbf{X}}_{u,n} = \left[\left(\left(\mathbf{G}_n^{\dagger}\cdot\mathbf{G}_n\right) + \sigma_{\mathrm{w}}^2\cdot\mathbf{I}\right)^{-1} \cdot \left(\mathbf{G}_n^{\dagger}\cdot\mathbf{r}_n\right)\right] \cdot \mathbf{W}_N \quad (24)$$

where $\mathbf{G}_n \in \mathbb{C}^{M\times M}$, $\mathbf{I}^{M\times M}$ is the identity matrix. This process indicates that for n-th block, we obtain the estimated $\hat{\mathbf{X}}_n^{M\times 1}$. After applying (23) to the detected $\hat{\mathbf{X}}_{u,n}$ in (24) and ZP removal, the decision to the nearest QAM symbol $\mathcal{D}\left(\hat{X}(m,n)\right)$ is made. Lastly, for the MFGS detector, the resultant $\hat{\mathbf{X}}_u$ from the initial iteration is passed though the recovery process to identify the desired $\mathbf{P}_{\mathrm{v}}$ vector. Next, the iteration process is applied forward. In other words, Gauss Seidel (GS) iteration is exercised on the matched filtered channel blocks $\mathbf{R}_n = \mathbf{G}_n^{\dagger}\cdot\mathbf{G}_n$. After the matched filtering operation, the input-output relation matrix in (18) is formulated as

$$\mathbf{z}_n = \mathbf{R}_n \cdot \mathbf{s}_{u,n} + \bar{\mathbf{w}}_n \quad (25)$$

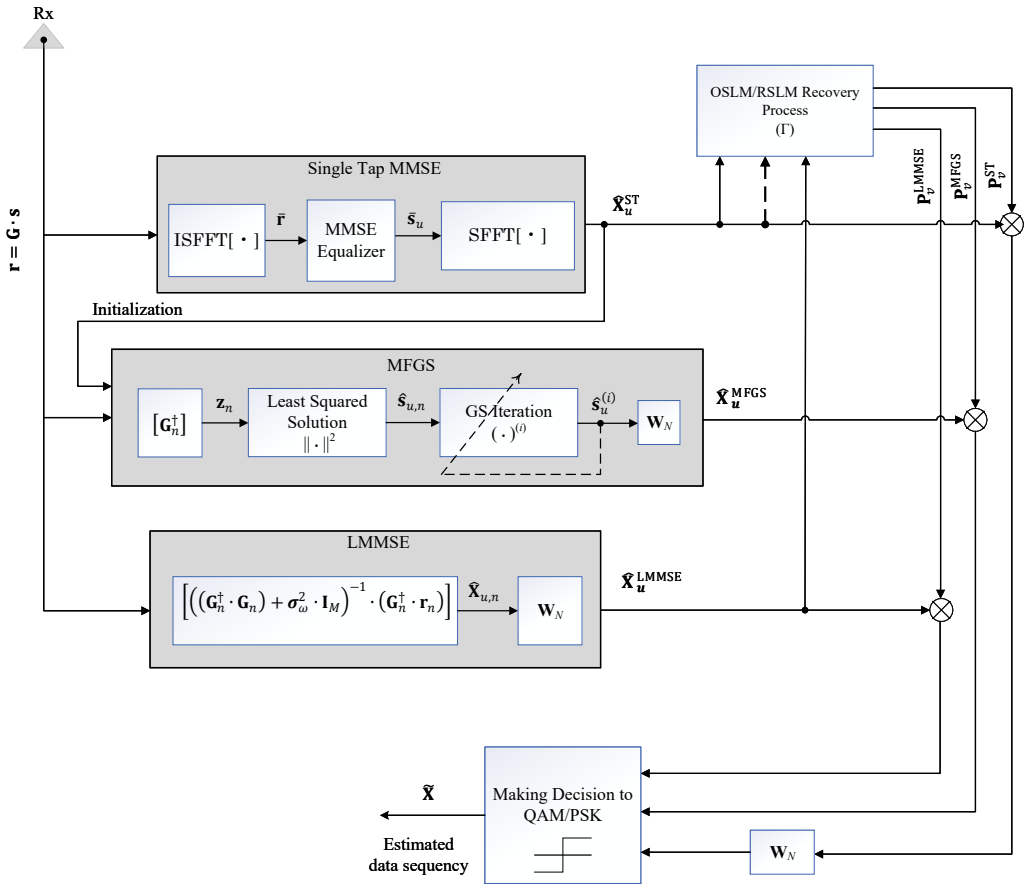

Fig. 4. The block diagram of the proposed OTSM receiver.

where $\mathbf{z}_n = \mathbf{G}_n^{\dagger} \cdot \mathbf{r}_n$ and $\bar{\mathbf{w}}_n = \mathbf{G}_n^{\dagger} \cdot \mathbf{w}_n$. The GS method is then used to iteratively find the least squares solution of the M-dimensional linear system in (25) as

$$\hat{\mathbf{s}}_{u,n} = \min_{\mathbf{s}_{u,n}} \|\mathbf{z}_n - \mathbf{R}_n \cdot \mathbf{s}_{u,n}\|^2. \tag{26}$$

Now, if we introduce the diagonal elements matrix as $\mathbf{D}_n$ and the strictly lower triangular elements matrix as $\mathbf{L}_n$ of the matrix $\mathbf{R}_n$, then, by applying the GS iterative algorithm to estimate $\mathbf{s}_n$ per i-th iteration, we get

$$\hat{\mathbf{s}}_{u,n}^{(i)} = -\mathbf{T}_n \cdot \hat{\mathbf{s}}_{u,n}^{(i-1)} + \mathbf{b}_n \tag{27}$$

where $\mathbf{b}_n = (\mathbf{D}_n + \mathbf{L}_n)^{-1} \cdot \mathbf{z}_n$, $\mathbf{T}_n = (\mathbf{D}_n + \mathbf{L}_n)^{-1} \cdot \mathbf{L}_n^{\dagger}$ and $\mathbf{T}_n \in \mathbb{C}^{M \times M}$ is the GS iteration matrix [3]. Note that the vector $\hat{\mathbf{s}}_{u,n}^{(i)} \in \mathbb{C}^{M \times 1}$ forms the transmitted samples in the time domain, after the estimation process, of the n-th block in the i-th iteration. Hence, the information symbols, in the delay-sequency domain, in the i-th iteration, are then given as follows

$$\hat{\mathbf{X}}^{(i)} = \mathcal{D}\left(\frac{\hat{\mathbf{X}}_u^{(i)}}{\mathbf{P}_{\mathrm{v}}}\right) = \mathcal{D}\left(\frac{\hat{\mathbf{s}}_u^{(i)} \cdot \mathbf{W}_N}{\mathbf{P}_{\mathrm{v}}}\right) \tag{28}$$

where $\hat{\mathbf{s}}_u^{(i)} = \left[\hat{\mathbf{s}}_{u,0}^{(i)}, \hat{\mathbf{s}}_{u,1}^{(i)}, \ldots, \hat{\mathbf{s}}_{u,N-1}^{(i)}\right]$ and $\mathcal{D}(\cdot)$ denotes the decision making function to the nearest QAM point.

Additionally, the time domain estimate is updated, for the next iteration, by back-warding the hard decision estimates to the time domain as follows [2–4]

$$\hat{\mathbf{s}}_u^{(i)} \leftarrow (1-\delta)\,\hat{\mathbf{s}}_u^{(i)} + \delta \mathrm{vec}\left(\mathbf{X}_u^{(i)} \cdot \mathbf{W}_N\right) \tag{29}$$

where δ indicates to the relaxation parameter which is modified when using a high constellation mapping size of the modulation, like 64-QAM and above [2–4, 25]. This proposed system is implemented with all these three detectors under assumption of non-coded technique and perfect channel state information.

3. Simulation Results and Discussion

In this section, we provide the OTSM system with OSLM/RSLM PAPR reduction. The simulation code (MATLAB-R2023b) of [2], [3] was modified and used in this study to include the PAPR reduction and recovery of both OSLM and RSLM schemes. Table 1 illustrates all input factors that have been implemented for the simulation. For any pulse shaping waveform, the OTSM signal is considered to be critically sampled, i.e., assuming that $T\Delta f = 1$. Also, a perfect channel state information is assumed, and channel is supposed to be under-spread, i.e., $\tau_{\max}\nu_{\max} \ll 1$.

Input factor	Abbreviation of factor	Value of the factor
The sub-carrier spacing	Δf	15 kHz
Total OTSM frame duration	T_{f}	$NT = N/\Delta f$
Total OTSM frame bandwidth	B	$M\Delta f = M/T$
Carrier frequency	f_{c}	4×10^9
Max. delay spread normalized to the receiver delay resolution	$l_{\max}$	$\leq M$
One delay tap	τ_i	$1/(M\Delta f)$
One Doppler tap	ν_i	$1/(NT)$
EPA Channel delay model	delays	$[0\ 30\ 70\ 90\ 110\ 190\ 410] \times 10^{(-9)}$
EPA power delay profile	pdp	$[0\ -1.0\ -2.0\ -3.0\ -8.0\ -17.2\ -20.8]$
EVA Channel delay model	delays	$[0\ 30\ 150\ 310\ 370\ 710\ 1090\ 1730\ 2510] \times 10^{(-9)}$
EVA power delay profile	pdp	$[0\ -1.5\ -1.4\ -3.6\ -0.6\ -9.1\ -7.0\ -12.0\ -16.9]$
ETU Channel delay model	delays	$[0\ 50\ 120\ 200\ 230\ 500\ 1600\ 2300\ 5000] \times 10^{(-9)}$
ETU power delay profile	pdp	$[-1\ -1\ -1\ 0\ 0\ 0\ -3\ -5\ -7\ ]$
No. of RSLM subvectos/block	V	M/U
No. of RSLM extended elements/subvector	α	2

Tab. 1. Input factors used in the simulation process of the proposal.

The standards EPA, EVA and ETU channel models are generated as described in the table. For the generated OSLM phase vectors, which is taken from the N-WHM, the first row was excluded because it introduces non phase modifications (i.e., the original phases of data symbols). Notice that the obtained CCDF-PAPR simulation results have been referenced to the theoretical curve of the distortionless PAPR reduction techniques, i.e. SLM/PTS, which shows the best characterization of PAPR at specific U phase vectors and $N \times M$ Delay-Sequency matrix. Last but not least, it is worth mentioning that due to the large number of factors (variables) that affect the PAPR/BER performances and to eliminate number of figures, the number of attempts for those variables was shortened. For example, but not limited to, $M \times N$ matrix size, number of candidate phase vector U, IBO of the PA, values of extension factors C and f, model of channel, size of constellation (M-QAM), user velocity, etc.

3.1 PAPR Reduction Results

From Fig. 5, at $N = M = 16$ of 16-QAM OTSM, we can observe that both the OSLM and RSLM schemes participate in reducing the PAPR. Precisely, RSLM performs better than OSLM due to the composition of OSLM, where its elements are distributed orthogonally from one vector to the other. Hence, the OSLM combination increases the chances of similarity between vectors (i.e., more correlation), unlike the case of RSLM, where its elements are randomly distributed (i.e., less correlation). In addition to that, because the OTSM system depends, essentially, on the WHT matrix, to transfer the delay-sequency symbols to delay-time, hence, the OSLM effect on PAPR will be rather smaller than RSLM effect. Ultimately, OSLM just means swapping the rows/columns in the WHT matrix between each other. It is worth mentioning that the PAPR-OSLM performance gets better when applying the ISFFT transform, $\mathbf{F}_N$, instead of WHT $\mathbf{W}_N$ as shown in Fig. 5(a) with $N = M$ and Figs. 6(a) and 6(b) when $N \neq M$, taking into consideration that the OTSM system performances (BER) with $\mathbf{W}_N$ and $\mathbf{F}_N$ are identical, as has been proven in [2, 3, 25]. The obtained results show that OSLM with $\mathbf{F}_N$ gains about 2 dB over OSLM with $\mathbf{W}_N$ at CCDF-PAPR of 10^{-4}. Also, from the provided PAPR figures, the RSLM scheme performs almost identical to the theoretical SLM curve, which reduces the PAPR about 3 dB from the non- PAPR reduction (the curve of the original PAPR data), at CCDF-PAPR of 10^{-4}.

Remark Some variables will not affect the performance of PAPR, if being changed. For instance, the size and type of constellation mapping (M-QAM, M-PSK, ... etc.) where all perform identical. Also, the value of extension factor will not affect the performance of CCDF-PAPR, if it is considered within the appropriate range (i.e. not causing a high shifting/clipping that leads to inter-modulation interference). Mainly, for a specific multi-carrier system (e.g., OFDM, OTSM, OTFS, ... etc.), CCDF-PAPR performance can be affected by varying either the number of generated phase vectors U and/or the DS matrix size $M \times N$.

3.2 System Performance

The effect of receiver's velocity and channel models on the system performance has been tested. The measurements of bit-error rate (BER) and side-information-error rate (SIER) have been illustrated, when applying the proposed OSLM and RSLM schemes in the presence of the non-linear power amplifier (SSPA) at different user's speed (Fig. 7 and Fig. 8) and channel models (Fig. 9). Altogether have been simulated with the proposed detectors (MFGS, LMMSE and ST-MMSE). SIER test measures the performance of recovery process. Side information error means that all symbols per an OTSM frame are lost due to the error recovery. In other words, SIER is counted when the OSLM/RSLM vector is detected wrongly such that the recovery vector $\mathbf{P}_{\mathrm{v}}$ is not match the desired one, and, as a result, the DS frame is converted to wrong phases causing a frame error.

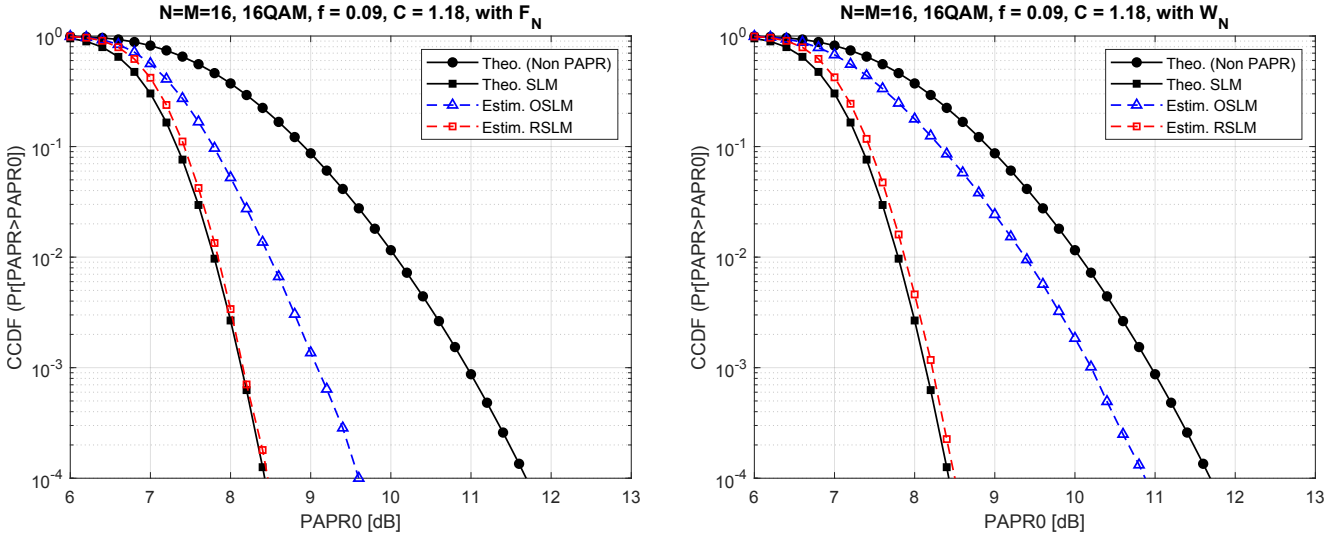

Fig. 5. CCDF-PAPR performances of the original delay-time data (i.e., without PAPR reduction) and with OSLM/RSLM schemes at $M = N$, $U = 6$ phase vectors and 16-QAM, when applying $\mathbf{F}_N$ and $\mathbf{W}_N$ transforms with $f = 0.09$ and $C = 0.18$.

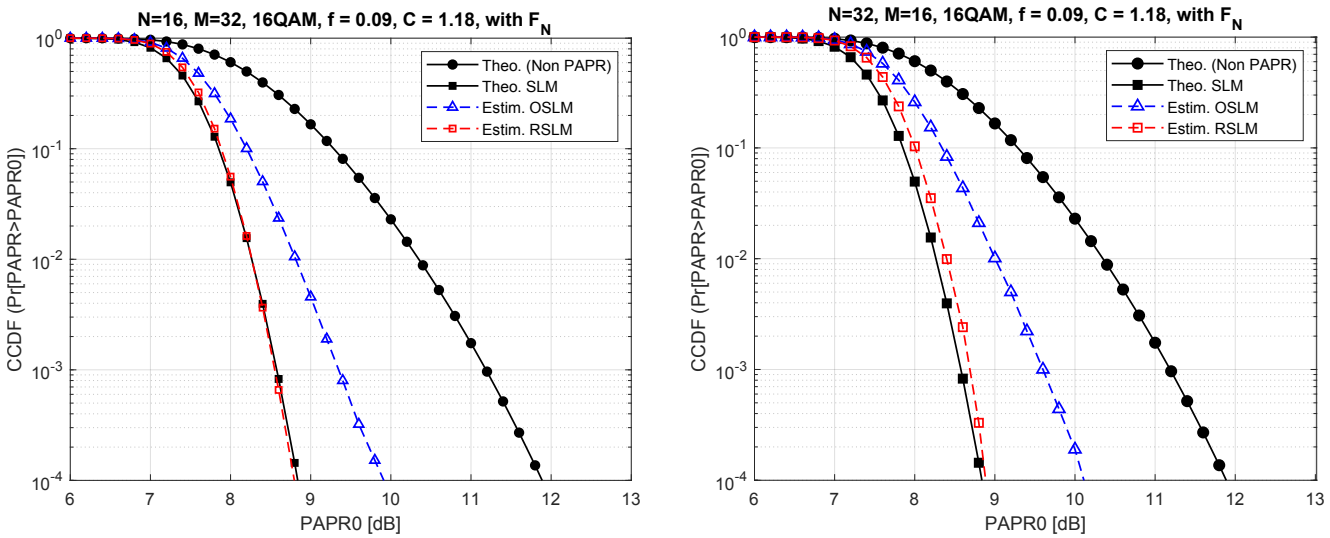

Fig. 6. CCDF-PAPR performances of the original delay-time data (i.e., without PAPR reduction) and with OSLM/RSLM schemes at $M \neq N$, $U = 6$ phase vectors and 16-QAM, when applying $\mathbf{F}_N$ transforms with $f = 0.09$ and $C = 0.18$.

Accordingly, Figure 7 shows the SIER of OSLM and RSLM recovery for 4-QAM in Fig. 7(a) and 16-QAM in Fig. 7(b), where $N = M = 32$, IBO = 5 dB and receiver's speed of 150 and 500 km/h. It can be observed that the performance becomes worse when increasing velocity of the receiver to 500 km/h, for both sizes of constellations. However, SIER of OSLM is still superior to RSLM for both cases although performances of OSLM at 500 km/h is much better than that at 150 km/h, for all kinds of provided detectors. This benefit is due to the structure of the OTSM which depends on the WHT matrix, such that the effect of the OSLM lies only in changing the location of one row/column to another inside the WHT matrix. For detectors performances, the LMMSE detector with 16-QAM provides the best performances for OSLM at both velocities while the MFGS detector suffers from errors in both 4-QAM and 16-QAM and shows the worst performances, especially with the RSLM scheme. On the other hand, in Fig. 8(a), BER is provided with 4-QAM and receiver's speed of 150 km/h while receiver's speed of 500 km/h is simulated in Fig. 8(b). Both were created with $N = M = 32$, IBO = 5 dB, $f = 0.09$ and $C = 0.18$ and EPA channel model. Accordingly, the effect of high speed appears negatively, especially with the ST-MMSE detector which is extremely decayed at 500 km/h speed. In addition, the LMMSE detector shows the superior performance for both OSLM and RSLM at both speeds, while the MFGS de-

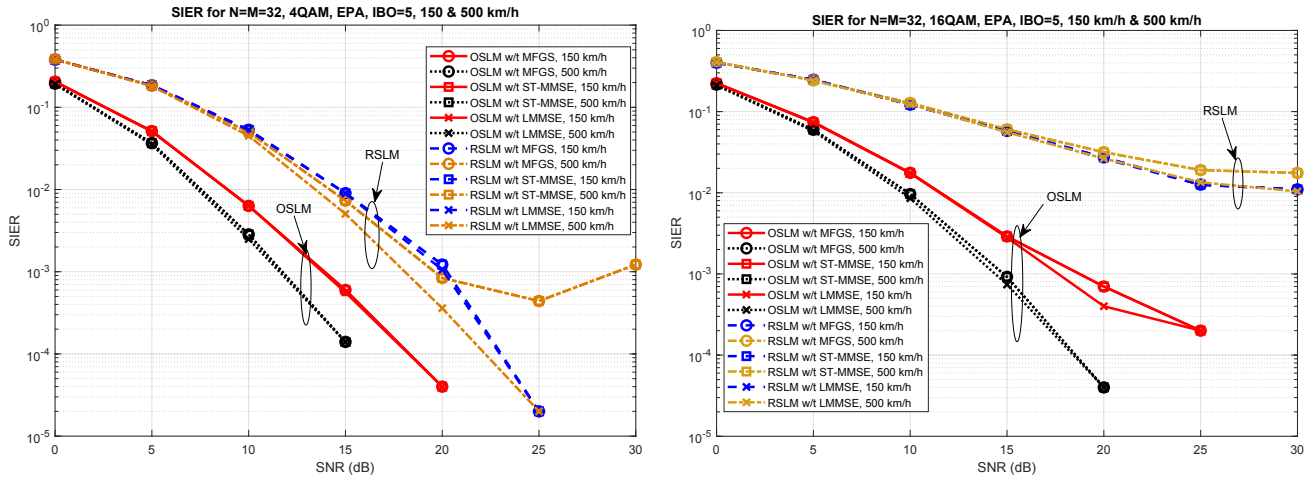

(a) (b)

Fig. 7. SIER of 4- and 16-QAM OTSM frame with OSLM and RSLM schemes at $M = N = 32$, $U = 4$, IBO = 5 dB, $f = 0.09$ and $C = 0.18$, with EPA channel model and user speed of 150 and 500 km/h.

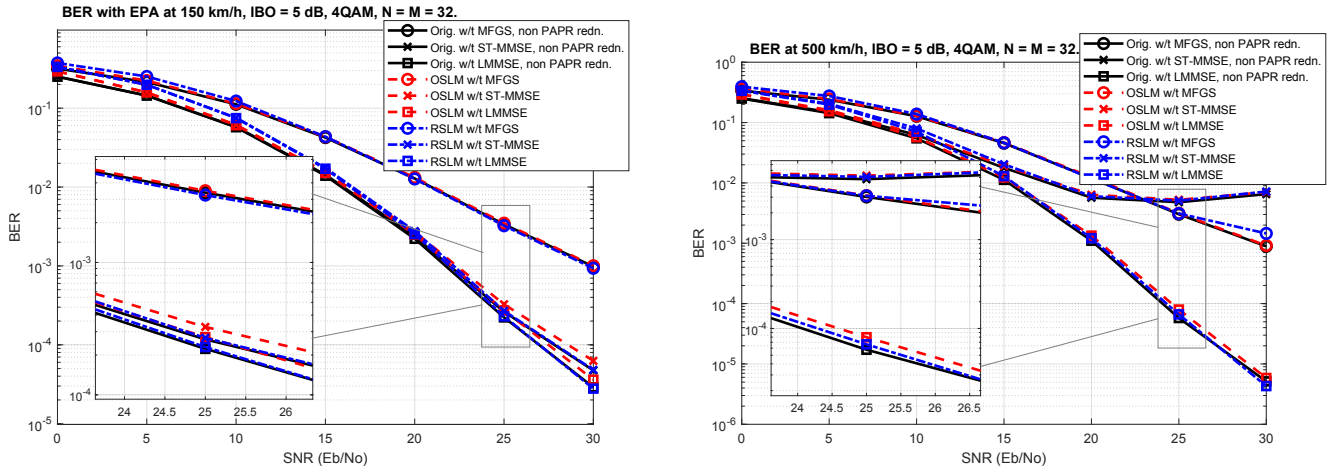

(a) (b)

Fig. 8. BER performances of the OTSM frame without PAPR reduction, with OSLM and with RSLM schemes at $M = N = 32$, $U = 4$, IBO = 5 dB, $f = 0.09$ and $C = 0.18$, with EPA channel model, at different size of QAM constellation and the speed of user (150 and 500) km/h.

tector shows the worst case. We can observe that, in these scenarios, the curves of both OSLM and RSLM mostly follow the curves of the original detectors, indicating that the main impact on the performance results from the detector itself, and not from the proposed OSLM and RSLM schemes.

At the conclusion of this section, a comparison between the proposed OSLM and RSLM schemes in the presence of EPA, EVA and ETU channel models is presented, by studying BER (Fig. 9(a)) and SIER (Fig. 9(b)). To implement this study, the LMMSE detector was considered with $M = N = 32$, IBO = 5 dB, $f = 0.09$, $C = 0.18$, and user's speed of 150 km/h. From Fig. 9(a), it can be observed that the channel model of ETU produces the lowest effect, which means that the BER performances of original phases and OSLM/RSLM in the presence of ETU model channel are the best, compared to performances when other channel models are applied. This fact is proven by the SIER performance in Fig. 9(b). It can be observed that the SIER of OSLM outperforms RSLM in all available channel models. The worst BER and SIER are also demonstrated with the EPA model, which means that this type of channel model introduces the highest negative impact on the transmitted OTSM frame.

Finally, Figure 10 shows the BER performance of the proposed OTSM with OSLM/RSLM when applying the single-tap detector for the AWGN channel and the multipath fading channel. The 4-QAM OTSM was simulated with $N = M = 32$ delay-sequency symbols, IBO = 5 dB, $U = 4$ candidate phase vectors, $f = 0.09$ and $C = 2f = 0.18$, at speed of 150 km/h. From the figure, it can be observed that the system performance of OSLM/RSLM is almost identical to the original one, for both scenarios of channels, AWGN and multipath fading.

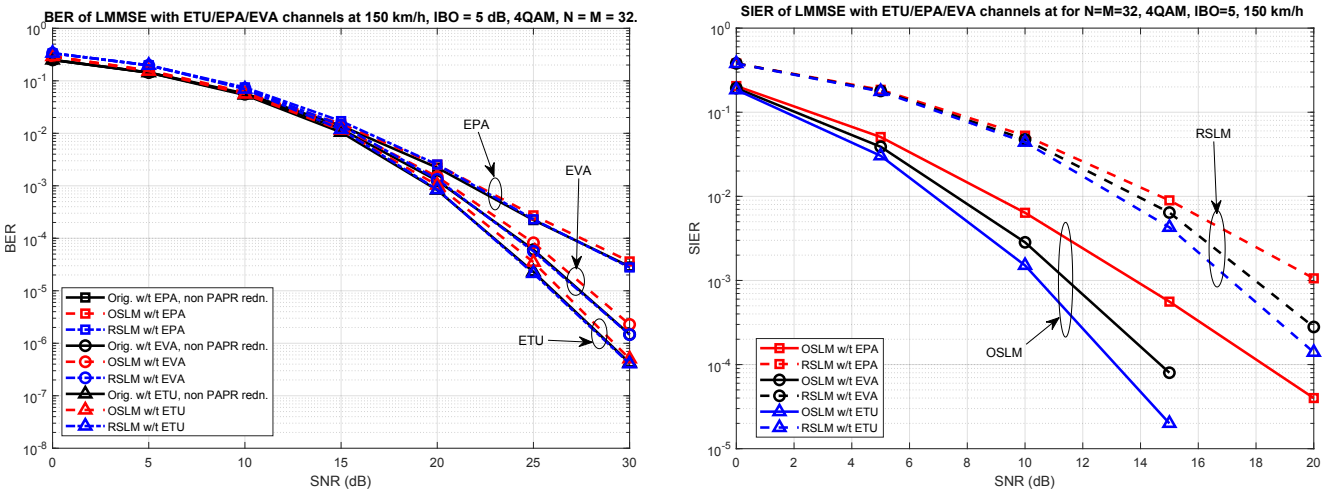

(a) (b)

Fig. 9. Performances of 4-QAM OTSM frame in terms of (a) BER and (b) SIER without PAPR reduction, with OSLM and with RSLM schemes at $M = N = 32$, $U = 4$, IBO = 5 dB, $f = 0.09$ and $C = 0.18$, with EPA/EVA/ETU channel models and user speed of 150 km/h.

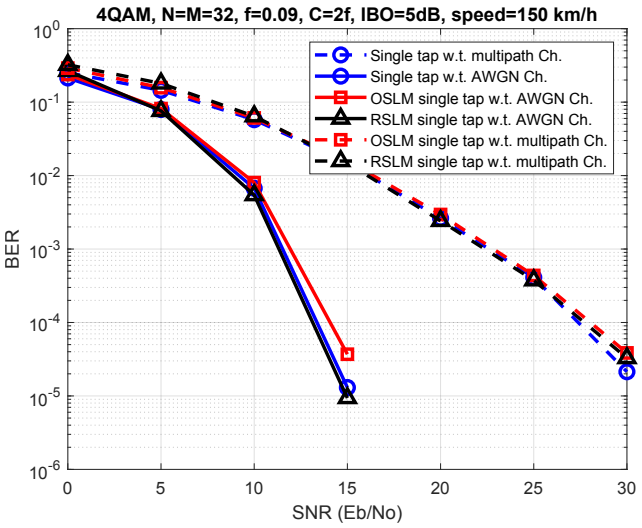

Fig. 10. BER performance of the single-tap detector for AWGN and multi-path fading channels with 4-QAM, $N = M = 32$, IBO = 5 dB, $U = 4$, $f = 0.09$, $C = 0.18$, at speed of 150 km/h.

3.3 Computational Complexity

It is well known that the source of computational complexity is, mainly, from the operations of OTSM, which includes inverse symplectic fast Fourier transform (ISFFT) and Heisenberg transform (IFFT). These operations can be considered as the reference of the computational complexity where the total number of complex multiplications and additions to compute all $(N \times M)$ samples via ISFFT and Heisenberg processes is $NM \log_2 (NM)$. Hence, by considering U candidate phase vector of SLM scheme, the computational complexity of ISFFT and Heisenberg operations will grow upto $UNM \log_2 (NM)$. Notice that the OTSM modulation, which is considered in this manuscript, introduces a low complexity at the detectors while maintaining the BER performance, as proposed by [1–3].

4. Conclusions

In this work, we have proposed reliable PAPR minimization methods based on OSLM and RSLM after modifying the OTSM transceiver construction. The power efficiency is discussed and it is shown that the extended factors, f and C, can be modified by a fractional value while maintaining the OTSM power efficiency. Also, we have tested the proposed OSLM and RSLM in terms of CCDF-PAPR, BER and SIER characteristics, in the presence of SSPA power amplifier, EPA, EVA and ETU channel models, and single tap-MMSE, MFGS and LMMSE detectors, including recovery process with different speeds of the user. The results of these tests show satisfactory PAPR performance especially for RSLM (which matches the theoretical curve of SLM CCDF-PAPR compared to the original curve). In addition, the BER and SIER performances are identical or very close to the reference (original) curves (which are not subject to the PAPR reduction process), for most tests.

Acknowledgments

This research was funded by the Researchers Supporting Project (no. RSP2024R484), King Saud University, Riyadh, Saudi Arabia.

References

[1] HARMUTH, H. F. Applications of Walsh functions in communications. *Spectrum*, 1969, vol. 6, no. 11, p. 82–91. DOI: 10.1109/MSPEC.1969.5214175

[2] THAJ, T., VITERBO, E., HONG, Y. Orthogonal time sequency multiplexing modulation: Analysis and low-complexity receiver design.

Transactions on Wireless Communications, 2021, vol. 20, no. 12, p. 7842–7855. DOI: 10.1109/TWC.2021.3088479

[3] THAJ, T., VITERBO, E. Orthogonal time sequency multiplexing modulation. In *IEEE Wireless Communications and Networking Conference (WCNC)*. Nanjing (China), 2021, p. 1–7. DOI: 10.1109/WCNC49053.2021.9417451

[4] HARMUTH, H. F. *Delay-Doppler Communications Principles and Applications*. 1st ed. Academic Press, 2022. ISBN: 9780323850285

[5] MOHAMMED, S. K. Derivation of OTFS modulation from first principles. *IEEE Transactions on Vehicular Technology*, 2021, vol. 70, no. 8, p. 7619–7636. DOI: 10.1109/TVT.2021.3069913

[6] REDDY, B., VELAMPALLI, C., DAS, S. Performance analysis of multi-user OTFS, OTSM, and single carrier in uplink. *IEEE Transactions on Communications*, 2024, vol. 72, no. 3, p. 1428–1443. DOI: 10.1109/TCOMM.2023.3332865

[7] KUMAR, A., SHARMA, H., GAUR, N., et al. PAPR analysis in OTFS using the centre phase sequence matrix based PTS method. *Results in Optics*, 2024, vol. 15, p. 1–8. DOI: 10.1016/J.RIO.2024.100664

[8] SURABHI, G. D., AUGUSTINE, R. M., CHOCKALINGAM, A. Peak-to-average power ratio of OTFS modulation. *IEEE Communications Letters*, 2019, vol. 23, no. 6, p. 999–1002. DOI: 10.1109/LCOMM.2019.2914042

[9] DOOSTI-AREF, A., MASOUROS, C., BASAR, E., et al. Pairwise sequency index modulation with OTSM for Green and robust single-carrier communications. *IEEE Wireless Communications Letters*, 2024, vol. 13, no. 4, p. 1083–1087. DOI: 10.1109/LWC.2024.3360256

[10] NAVEEN, C., SUDHA, V. Peak-to-average power ratio reduction in OTFS modulation using companding technique. In *The 5th International Conference on Devices, Circuits and Systems (ICDCS)*. Coimbatore (India), 2020, p. 140–143. DOI: 10.1109/ICDCS48716.2020.243567

[11] AL AHSAN, R., GHANNOUCHI, F. M., FAPOJUWO, A. O. Analysis of adapted tone reservation PAPR reduction techniques in OTSM system. In *The 33rd International Telecommunication Networks and Applications Conference*. Melbourne (Australia), 2023, p. 162–168. DOI: 10.1109/ITNAC59571.2023.10368554

[12] NEELAM, S. G., SAHU, P. R. Iterative channel estimation and data detection of OTSM with superimposed pilot scheme and PAPR analysis. *IEEE Communications Letters*, 2023, vol. 27, no. 8, p. 2147–2151. DOI: 10.1109/LCOMM.2023.3281575

[13] KALPAGE, N. V., PRIYA, P., HONG, Y. DCT-based OTFS with reduced PAPR. *Communications Letters*, 2024, vol. 28, no. 1, p. 158–162. DOI: 10.1109/LCOMM.2023.3337778

[14] WANG, Z., CHEN, X., SUN, Z., et al. On the performance of nonlinear corrective active constellation expansion in OTFS systems. *IEEE Communications Letters*, 2022, vol. 26, no. 6, p. 1418–1422. DOI: 10.1109/LCOMM.2022.3165191

[15] SHANG, H., CHEN, R., ZHANG, H., et al. OTFS modulation and PAPR reduction for IoT-railways. *China Communications*, 2023, vol. 20, no. 1, p. 102–113. DOI: 10.23919/JCC.2023.01.009

[16] GAO, S., ZHENG, J. Peak-to-average power ratio reduction in pilot-embedded OTFS modulation through iterative clipping and filtering. *IEEE Communications Letters*, 2020, vol. 24, no. 9, p. 2055–2059. DOI: 10.1109/LCOMM.2020.2993036

[17] TEK, Y. I., BASAR, E. PAPR reduction precoding for orthogonal time frequency space modulation. In *The 46th International Conference on Telecommunications and Signal Processing (TSP)*. Prague (Czech Republic), 2023, p. 172–176. DOI: 10.1109/TSP59544.2023.10197718

[18] SU, J., LIU, S., HUANG, Y., et al. Peak-to-average power ratio reduction via symbol precoding in OTFS modulation. In *IEEE 95th Vehicular Technology Conference (VTC2022-Spring)*. Helsinki (Finland), 2022, p. 1–5. DOI: 10.1109/VTC2022-Spring54318.2022.9860629

[19] BAENA-LECUYER, V., ORIA ORIA, A. C., GRANADO ROMERO, J. Low PAPR preamble-based channel estimation for OTFS systems on static multipath channels. *Digital Signal Processing*, 2023, vol. 136, p. 1–7. DOI: 10.1016/J.DSP.2023.103979

[20] BAI, J., LIN, B., TAO, X. Improved PAPR reduction algorithm for OTFS systems. In *The 19th International Conference on Natural Computation, Fuzzy Systems and Knowledge Discovery (ICNC-FSKD)*. Harbin (China), 2023, p. 1–6. DOI: 10.1109/ICNC-FSKD59587.2023.10281178

[21] CHENNAMSETTY, S., BODDU, S., CHANDHAR, P. , et al. Analysis of PAPR in OTFS modulation with classical selected mapping technique. In *The 15th International Conference on COMmunication Systems and Networks (COMSNETS)*. Bangalore (India), 2023, p. 319–322. DOI: 10.1109/COMSNETS56262.2023.10041313

[22] SHARMA, S., SHAH, S. W. H., WIDMER, J. A low-complexity standard-compliant PAPR reduction scheme for OTFS modulation. In *IEEE 99th Vehicular Technology Conference (VTC2024-Spring)*. Singapore, 2024, p. 1–7. DOI: 10.1109/VTC2024-Spring62846.2024.10683635

[23] ASSERI, M. I., TSIMENIDIS, C. C., SHARIF, B. S., et al. Orthogonal-SLM technique for PAPR reduction and recovery without side information in OFDM systems. In *The 7th International Symposium on Communication Systems, Networks and Digital Signal Processing (CSNDSP)*. Newcastle upon Tyne (UK), 2010, p. 162–166. DOI: 10.1109/CSNDSP16145.2010.5580440

[24] LE GOFF, S. Y., KHOO, B. K., TSIMENIDIS, C. C., et al. A novel selected mapping technique for PAPR reduction in OFDM systems. *IEEE Transactions on Communications*, 2008, vol. 56, no. 11, p. 1775–1779. DOI: 10.1109/TCOMM.2008.070021

[25] THAJ, T., VITERBO, E. Low complexity iterative rake decision feedback equalizer for zero-padded OTFS systems. *IEEE Transactions on Vehicular Technology*, 2020, vol. 69, no. 12, p. 15606–15622. DOI: 10.1109/TVT.2020.3044276

[26] BJORCK, A. *Numerical Methods for Least Squares Problems*. SIAM, 1996. DOI: 10.1137/1.9781611971484

[27] DUDAK, C., KOC, A. T., KOC, S. Solid state power amplifier (SSPA) nonlinearity effects on quadri-phase shift keying modulation. In *The 7th European Conference on Wireless Technology*. Amsterdam (Netherlands), 2004, p. 237–240. ISBN: 1580539912

[28] STRAUSS, R. Reliability of SSPA's and TWTA's. *IEEE Transactions on Electron Devices*, 1994, vol. 41, no. 4, p. 625–626. DOI: 10.1109/16.278524

About the Author

Mohammed AL-RAYIF holds a bachelor's degree in Electrical Engineering from King Saud University, Riyadh, Saudi Arabia in the field of Electrical Engineering. He received his MSc. and Ph.D. degrees from Newcastle University, UK in 2006 and 2010 respectively in Communications and Signal Processing. From 1998 to 2014, he held several positions in the General Directorate of Border Guards in the Ministry of Interior in the Kingdom of Saudi Arabia, including for example the Head of Wired/Wireless Systems Department

(2000–2003) and Director of Communications Systems in the Border Guards (2011–2013). He served as Chairman of the Electrical Engineering Department and Vice Dean of the College of Engineering at King Khalid University in Ahab (2014–2017). During the period 2018–2019, he was a collaborating faculty member with the Department of Applied Electrical Engineering, Al-Muzahimiyah branch, King Saud University. Mohamed Al-Rayif has been working since 2019 as an Associate Professor in the Department of Applied Electrical Engineering. His research interests include OFDM, MIMO, OTSM/OTFM systems, artificial intelligence techniques, mm wave communications. Mohammed Al-Rayif has contributed his research publications to many prestigious international journals and conferences.